PNAS Nexus, 2022, 1, 1–8
https://doi.org/10.1093/pnasnexus/pgac116
Advance access publication date: 11 July 2022
Research Report

Structural basis of unisite catalysis of bacterial F_0F_1-ATPase

Atsuki Nakano[a], Jun-ichi Kishikawa[a,b], Atsuko Nakanishi[a,c], Kaoru Mitsuoka[c] and Ken Yokoyama[a,*]

[a]Department of Molecular Biosciences, Kyoto Sangyo University, Kamigamo-Motoyama, Kita-ku, Kyoto 603-8555, Japan
[b]Institute for Protein Research, Osaka University, 3-2 Yamadaoka, Suita, Osaka 565-0871, Japan
[c]Research Center for Ultra-High Voltage Electron Microscopy, Osaka University, 7-1 Mihogaoka, Ibaraki, Osaka 567-0047, Japan
*To whom correspondence may be addressed: Email: yokoken@cc.kyoto-su.ac.jp
Edited By: Shibu Yooseph

Abstract

Adenosine triphosphate (ATP) synthases (F_0F_1-ATPases) are crucial for all aerobic organisms. F_1, a water-soluble domain, can catalyze both the synthesis and hydrolysis of ATP with the rotation of the central $\gamma\varepsilon$ rotor inside a cylinder made of $\alpha_3\beta_3$ in three different conformations (referred to as β_E, β_{TP}, and β_{DP}). In this study, we determined multiple cryo-electron microscopy structures of bacterial F_0F_1 exposed to different reaction conditions. The structures of nucleotide-depleted F_0F_1 indicate that the ε subunit directly forces β_{TP} to adopt a closed form independent of the nucleotide binding to β_{TP}. The structure of F_0F_1 under conditions that permit only a single catalytic β subunit per enzyme to bind ATP is referred to as unisite catalysis and reveals that ATP hydrolysis unexpectedly occurs on β_{TP} instead of β_{DP}, where ATP hydrolysis proceeds in the steady-state catalysis of F_0F_1. This indicates that the unisite catalysis of bacterial F_0F_1 significantly differs from the kinetics of steady-state turnover with continuous rotation of the shaft.

Significance Statement:

The F_0F_1-ATPase rotates its central axis by continuously changing the structure of the three β subunits upon ATP hydrolysis. Here, we reconstructed cryo-electron microscopy structures under unisite conditions that permit only a single catalytic β subunit per enzyme to bind ATP. The structures indicated that hydrolysis of the first ATP occurs at β_{TP} instead of β_{DP}, where ATP hydrolysis proceeds in the steady-state catalysis of F_0F_1. This indicates that unisite catalysis is an initial reaction that is distinguished from steady-state rotary catalysis in F_0F_1.

Introduction

Adenosine triphosphate (ATP) synthases (F_0F_1) are crucial for aerobic organisms and reside in the inner membranes of mitochondria, plasma membranes of bacteria, and thylakoid membranes of chloroplasts in plants (1–3). F_0F_1 consists of a hydrophilic F_1 domain responsible for ATP hydrolysis or synthesis and a hydrophobic F_0 domain housing proton translocation across the membranes. ATP hydrolysis/synthesis in F_1 is coupled to proton flow in F_0 through the rotation of a common shaft.

F_0F_1 from the thermophilic bacteria *Geobacillus stearothermophilus* is one of the best characterized ATP synthases because of its structural stability and simple subunit structure ($\alpha_3\beta_3\gamma_1\varepsilon_1\delta_1a_1b_2c_{10}$; Fig. 1A). In particular, single-molecule rotation experiments using this enzyme enabled direct observation of the rotation of ATP synthase, which considerably improved our understanding of the mechanochemical cycle of F_0F_1 (4–11).

The $\gamma\varepsilon$ rotor in the F_1 domain ($\alpha_3\beta_3\gamma_1\delta_1\varepsilon_1$) is surrounded by a cylinder composed of three noncatalytic α and three catalytic β subunits arranged alternately (Fig. 1). The ε subunit modulates ATP hydrolysis activity by the structural change from a contracted to an extended form with a C-terminus helix towards $\alpha_3\beta_3$ (12). Several experimental studies have demonstrated that the extended C-terminus of the ε subunit (ε-CT up form) strongly inhibits ATPase activity of the F_1 domain; however, the inhibition mechanism of the ε-CT up form remains elusive.

In F_1 domain, six nucleotide-binding sites are located at different interfaces between the α and β subunits; three catalytic sites are located mainly in the β subunit, while the other three sites, called noncatalytic nucleotide-binding sites, are located mainly in the α subunit. According to the binding change mechanism of ATP synthesis, the three catalytic β subunits in F_1 are in different conformations (open, loose, and tight); However, they interconvert sequentially between three different conformations as catalysis proceeds (2). Thus, at a given time, all three catalytic β subunits are in different conformations. The crystal structure of F_1 from bovine heart mitochondria demonstrated the following asymmetry of catalytic sites: β_E, which adopts an open structure with no nucleotide; β_{TP}, which adopts a structure containing ATP analog (AMPPNP); and β_{DP}, which adopts a structure containing ADP (13, 14). The C-terminal region of each β subunit interacts with the γ subunit, and the differences are a consequence of the asymmetric association of the γ subunit with the $\alpha_3\beta_3$ cylinder. Thus, sequential interconversion between three different β subunits drives the rotation of the γ subunit with ATP hydrolysis (4).

Competing Interest: The authors declare no competing interests.
Received: June 15, 2022. **Accepted:** July 7, 2022

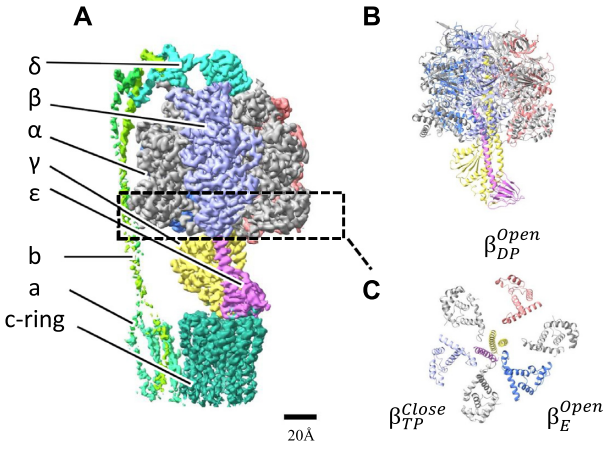

Fig. 1. Structure of nucleotide depleted wild-type F_0F_1 (*ND-wt-*F_0F_1) of *G. stearothermophilus*. Cryo-electron microscopy density map of *ND-wt-*F_0F_1 (state 1). (A) Side view of the overall structure of F_0F_1 as a ribbon model. All α subunits are represented as gray, and other subunits are colored in F_1 domain. (B) View of the F_0 side of F_1 domain at C terminal region. Superscript indicates the closed or open structure of the β subunit. (C) Ribbon representation of view from the F_0 side. No nucleotide was found at noncatalytic or catalytic nucleotide-binding sites.

The asymmetric structures of $\alpha_3\beta_3$ were found in the F_1 structure of other species (15–17) and V-ATPases (16), which is another rotary ATPase that is evolutionarily and structurally related to F_0F_1. In this study, we refer to the asymmetric architecture as a "Walker structure."

Assuming that F_0F_1 adopts the Walker structure during ATP hydrolysis, the alternating participation of β subunits within ATP hydrolysis does not require positive cooperation. Early studies showed that F_1-ATPases exhibited multiple K_m, likely due to the activation of F_1-ATPase by the binding of ATP to the α subunits (18). However, using both bulk and single-molecule experiments, one rotary mechanism was found to govern the entire range of nanomolar to millimolar ATP (19). This indicates that thermophilic F_1-ATPase obeys simple Michaelis–Menten kinetics with a single K_m value. However, previous experiments using a mitochondrial F_1 indicated strong positive cooperation between the catalytic sites. F_1-ATPase was compared under unisite and multisite catalytic conditions in which the ATP/enzyme ratio was adjusted to facilitate operation of either one or three sites (20). The multisite/unisite rate enhancement ratio of 10^6 fold was interpreted as a reflection of the strong positive cooperation among the three catalytic sites. The unisite catalysis experiment also suggests a high affinity of unisite to ATP with a binding constant K_d of $\sim 10^{-12}$ M, which is markedly higher than the K_m of $\sim 10^{-5}$ M in bacterial F_1 (19, 21). For thermophilic F_1-ATPase, similar ATP hydrolysis in a single catalytic site has been reported (21–23). However, the structural basis of the high affinity for ATP observed in unisite catalysis and whether unisite catalysis reflects steady-state activity (multisite catalysis) remains elusive.

In this study, we constructed a mutant F_0F_1 with a C-terminus-truncated ε subunit and showed that it does not undergo ε inhibition. The structure of this mutant F_0F_1 was determined using cryo-electron microscopy (cryo-EM) and compared with that of wild-type (*wt*) F_0F_1 to understand the structural basis of ε inhibition. Furthermore, we determined the structure of the mutant F_0F_1 under unisite catalytic conditions to capture the structure after ATP hydrolysis of the β subunit.

Results

Cryo grid preparation of *wt*-F_0F_1 and ATPase-active $\Delta\varepsilon$*CT*-F_0F_1

In this study, we used purified F_0F_1 from *G. stearothermophilus* expressed in *Escherichia coli* (24). The ATPase activity of *wt*-F_0F_1 is $\sim 10\ s^{-1}$ (Supplementary Fig. S1 and Supplementary Table S1), which is considerably lower than that of F_1 ($\alpha_3\beta_3\gamma$, $\sim 70\ s^{-1}$) (25). Several studies have indicated that ATP hydrolysis by *G. stearothermophilus* F_0F_1 is significantly inhibited when the extended C-terminal region of the ε subunit penetrates the $\alpha_3\beta_3$ cavity (12, 26–28). The initial ATPase activity of *wt*-F_0F_1 was very low because of the initial lag (Supplementary Fig. S1). To obtain ATPase-active F_0F_1, we constructed a mutant F_0F_1 with a C-terminal-truncated ε subunit ($\Delta\varepsilon$*CT*-F_0F_1). The prepared $\Delta\varepsilon$*CT*-F_0F_1 was subjected to dialysis in phosphate-buffered saline to deplete the bound nucleotide, as described in the *Materials and Methods* section. For the nucleotide-depleted thermophilic F_0F_1 (*ND-*$\Delta\varepsilon$*CT*-F_0F_1), the lag time was shorter than that of *wt*-F_0F_1, and the ATPase activity at 1,000 s after the start of reaction was $130\ s^{-1}$ (Supplementary Table S1), which was comparable to the ATPase activity of *wt*-F_1 without the ε subunit (5, 25).

First, we prepared a cryo grid of nucleotide-depleted *wt*-F_0F_1 (*ND-wt-*F_0F_1) in the absence or presence of 4 mM ATPγS. In addition, the cryo grid of $\Delta\varepsilon$*CT*-F_0F_1 under unisite conditions (molar ratio of enzyme to ATP is approximately 1:4.) was used for structural analysis. These cryo grids were subjected to cryo-EM image acquisition using a Titan Krios (Thermo Fisher Scientific) equipped with a K3 direct electron detector.

Structure of *ND-wt-*F_0F_1

Flowcharts showing the image acquisition and reconstitution of the 3D structure of nucleotide-depleted *wt*-F_0F_1 (*ND-wt-*F_0F_1) are summarized in Supplementary Fig. S2. We reconstructed three rotational states (state 1: 3.1 Å, state 2: 3.0 Å, and state 3: 3.7 Å resolutions) from the single-particle images of *ND-wt-*F_0F_1. The structure of *ND-wt-*F_1 domain is similar to the structure of F_1 domain in *wt*-F_0F_1 reported in a study by Guo et al.(6N2Y(12)), which adopted the following structures: "open in β_E without nucleotide," "closed in β_{TP} containing ADP," and "open in β_{DP} without nucleotide." In fact, the three β subunits in *ND-wt-*F_1 are similar to their counterparts in *wt*-F_0F_1 (Supplementary Fig. S3). In the structure of *ND-wt-*F_0F_1, the C-terminal helix of the ε subunit (ε-*CT*) also adopts the up form and penetrates the cavity of the $\alpha_3\beta_3$ cylinder (Fig. 1B). In contrast to the previous structure of *wt*-F_0F_1 (12), no nucleotide density was observed at the noncatalytic nucleotide-binding site in the three α subunits or the catalytic site in β_{TP} (Figs. 1C and 3A). Instead, a density likely corresponding to a phosphate was observed at the catalytic site of β_{TP} (Fig. 3A and Supplementary Fig. S4A). This phosphate was possibly derived from the phosphate buffer used for nucleotide depletion.

Therefore, the structure indicates that the closed structure of β_{TP} is stabilized by the penetration of ε-*CT* into the cavity between α_{DP} and β_{TP}, which is independent of nucleotide binding to β_{TP}.

Structure of *wt*-F_0F_1 exposed to 4 mM ATPγS

Previous studies have indicated that the binding of ATP to an isolated ε subunit induces a conformational change in ε-*CT* from the "up" to "down" form (25, 29). The ATPase activity of *wt*-F_0F_1 gradually accelerated in the presence of 4 mM ATP (Supplementary Fig. S1 and Supplementary Table S1). In this study, we determined the cryo-EM structure of F_0F_1 exposed to 4 mM ATPγS, which is a slow hydrolyzable ATP analog (30), to prove the conformational

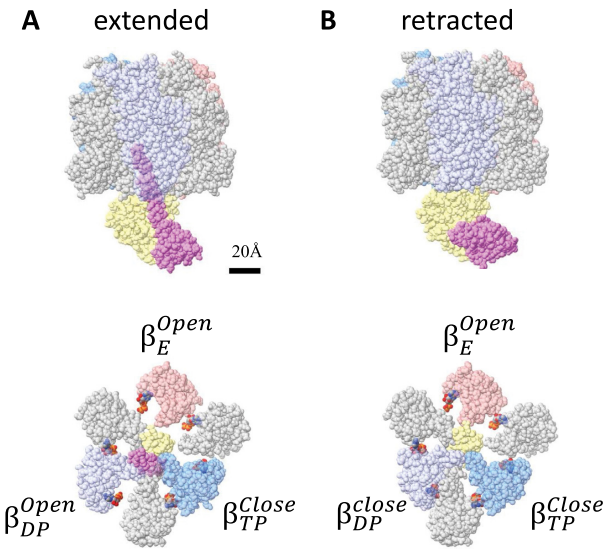

Fig. 2. Structure of wild-type F_0F_1 (*wt*-F_0F_1) exposed to 4 mM ATPγS. Structures of *wt*-F_0F_1 exposed to 4 mM ATPγS with the retracted (A) or extended (B) ε-subunit viewed from vertical side (upper) and from F_1 side (lower). The bound nucleotides are represented as color spheres. All α subunits are represented in gray, and all β subunits are colored.

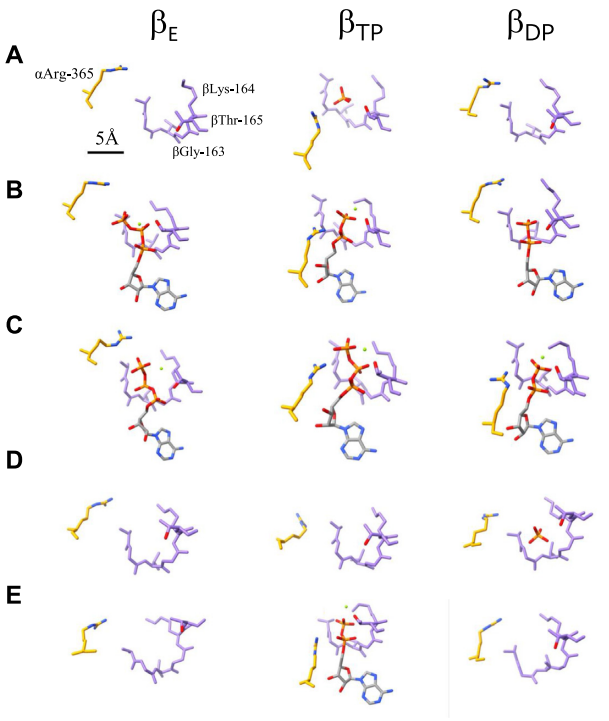

Fig. 3. Structure of catalytic sites of wild-type and mutated F_0F_1 under different condition. Magnified views of the three catalytic sites (β_E, β_{TP}, and β_{DP}) in each structure are shown as follows: (A) *ND-wt*-F_0F_1, (B) *wt*-F_0F_1 ε up form with ATPγS, (C) *wt*-F_0F_1 ε down form with ATPγS, (D) *ND*-Δ*CT*-F_0F_1, and (E) *US*-Δ*CT*-F_0F_1. Bound nucleotides and Mg ions are highlighted as stick and spherical representations, respectively. Scale bar is 5 Å.

change of the ε subunit in the complex. After focused 3D classification using a mask covering the F_1 domain (Supplementary Fig. S5B), we obtained the following two structures: F_1 with the up form of ε subunit from 526,524 particles at 2.6 Å resolution and F_1 with the down form of ε subunit from 39,991 particles at 3.3 Å resolution (Fig. 2 and Supplementary Fig. S5B). In the down form of ε subunit in the complex, the density of bound ATPγS was identified with similar coordination of surrounding amino acid residues to that in the monomeric ε subunit (Supplementary Fig. S6) (31). F_0F_1 with the down form of ε subunit adopted the following canonical Walker structures: "open in β_E with ATPγS," "closed in β_{TP} with ATPγS," and "closed in β_{DP} with ADP " (Figs. 2B and 3C). ATPγS molecules were also identified at the noncatalytic sites of the three α subunits (Fig. 2, lower). In contrast, the structure of F_0F_1 with the extended ε-*CT* was similar to the *ND-wt*-F_0F_1 structure, except the nucleotide occupancy of "open in β_E with ATPγS," "closed in β_{TP} with ADP," and "open in β_{DP} with ADP" (Fig. 3B). These results indicate that the extended ε-*CT* hampers the conformational change of the F_1 domain from the inhibitory conformation with "open in β_E," "closed in β_{TP}," and "open in β_{DP}" to the Walker structure with "open in β_E," "closed in β_{TP}," and "closed in β_{DP}" during ATP hydrolysis.

Structure of $\Delta\varepsilon$CT-F_0F_1 under unisite catalysis conditions

To capture the structure of the unisite catalysis of F_0F_1, 15 μM of *ND*-$\Delta\varepsilon$*CT*-F_0F_1 was mixed with 4 μM of the ATP-containing regeneration system described in the *Materials and Methods* section. The mixture was incubated for 120 s at 25°C, then loaded onto a holey grid, and subjected to flash freezing.

We obtained multiple F_0F_1 structures with and without nucleotides (*ND*-$\Delta\varepsilon$*CT*-F_0F_1) in the β_{TP} using 418,497 selected particle images of $\Delta\varepsilon$*CT*-F_0F_1 (Supplementary Fig. S7B). For *ND*-$\Delta\varepsilon$*CT*-F_0F_1, the structures of two rotational states without nucleotides were obtained at the following resolutions: state 1 at 3.6 Å and state 2 at 3.4 Å, with the γ subunit positions differing by 120° in each state. The structure of state 3 without nucleotides was not identified because of the small number of particles. Further, we obtained the F_1 parts of states 1 and 2 at resolutions of 3.4 Å and 3.3 Å, respectively, using focused refinement of the F_1 domain (Supplementary Fig. S7B).

The structure of *ND*-$\Delta\varepsilon$*CT*-F_0F_1 significantly differs from the structure of *ND-wt*-F_0F_1 in which three catalytic β subunits adopt "open in β_E," "closed in β_{TP}," and "open in β_{DP}" (Fig. 1C). In contrast, all three β subunits in *ND*-$\Delta\varepsilon$*CT*-F_0F_1 adopt an almost identical structure of open conformations as follows: "open in β_E," "open in β_{TP}," and "open in β_{DP}" (Fig. 4A). There was no nucleotide bound to the three open β subunits of *ND*-$\Delta\varepsilon$*CT*-F_0F_1, but a density corresponding to phosphate was observed in the β_{DP} (Fig. 3D and Supplementary Fig. S4D). This phosphate may be derived from the phosphate buffer used for nucleotide depletion. Our findings suggest that nucleotide depletion from the F_1 domain causes all three β subunits to adopt an open conformation. The interaction of the γ subunit with the three open β subunits are shown in Supplementary Fig. S8. The C termini region of closed β_{TP} is in close proximity to the coiled coil of the γ subunit, while the open β_{TP} is in close proximity to the globular domain of the γ subunit (Supplementary Fig. S8C).

In other words, the penetration of extended ε-*CT* into the $\alpha_3\beta_3$ cavity does not result in the open conformation of β_{DP} but rather forces open β_{TP} without bound nucleotides to the closed conformation (cf. Figs. 1C and 4A).

For *ND*-$\Delta\varepsilon$*CT*-F_0F_1 containing a nucleotide in β_{TP}, we determined the structures of the following three states: state 1 at 3.2 Å, state 2 at 3.4 Å, and state 3 at 4.0 Å. For state 1, another subclass with nearly identical structure (state 1) was isolated (Supplementary Fig. S6C). Upon focused refinement using an F_1 mask,

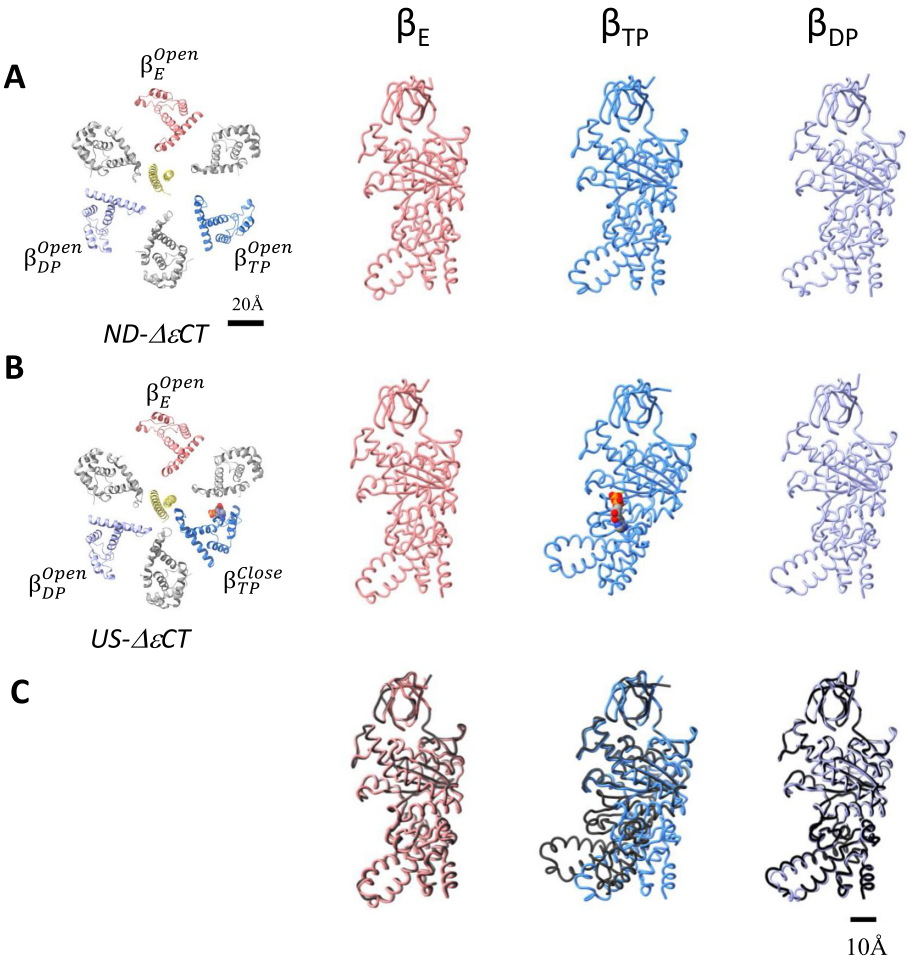

Fig. 4. Comparison of the structure of nucleotide-depleted $\Delta\varepsilon$*CT*-F_0F_1 with that of *US*-$\Delta\varepsilon$*CT*-F_0F_1. Cryo-electron microscopy structures of *ND*-$\Delta\varepsilon$*CT*-F_0F_1 (A) and $\Delta\varepsilon$*CT*-F_0F_1 under unisite conditions (B). The slice view of the F_1 domain is represented in the left panel, and the main chain of each β subunit is lined. *Right panels*, each β subunits (β_{TP}, β_{DP}, and β_E) of *ND*-$\Delta\varepsilon$*CT*-F_0F_1 or *US*-$\Delta\varepsilon$*CT*-F_0F_1 is represented as a colored chain. (C) Comparison of the β subunits between *ND*-$\Delta\varepsilon$*CT*-F_0F_1 and *US*-$\Delta\varepsilon$*CT*-F_0F_1. Each β subunit (β_{TP}, β_{DP}, and β_E) of *ND*-$\Delta\varepsilon$*CT*-F_0F_1(colored chain) or *US*-$\Delta\varepsilon$*CT*-F_0F_1 (black chain) is superimposed on the β-barrel domain (1 to 80 amino acids).

the structure of the F_1 domain for each state was obtained (Supplementary Fig. S6B, lower). We refer to the $\Delta\varepsilon$*CT*-F_0F_1 structure containing a nucleotide at the β_{TP} as UniSite-$\Delta\varepsilon$*CT*-F_0F_1 (*US*-$\Delta\varepsilon$*CT*-F_0F_1). The structure of *US*-$\Delta\varepsilon$*CT*-F_0F_1 was different from that of *ND*-$\Delta\varepsilon$*CT*-F_0F_1. The structures of two β subunits, β_E and β_{DP}, adopted an open form without nucleotides, whereas β_{TP} adopted a closed form containing nucleotide density (Fig. 3E). These findings indicate that the structure of *US*-$\Delta\varepsilon$*CT*-F_0F_1 is very similar to that of *ND*-*wt*-F_0F_1. Specifically, F_0F_1 in both structures adopt "open in β_E," "closed in β_{TP}," and "open in β_{DP}." In addition, the relative position of the γ subunit to $\alpha_3\beta_3$ was completely analogous in the two structures (Supplementary Fig. S9). The structure of *US*-$\Delta\varepsilon$*CT*-F_0F_1 revealed a nucleotide density due to ADP at the catalytic site in β_{TP}, indicating that ATP bound to β_{TP} was already hydrolyzed (Figs. 3E and 4B).

Furthermore, the position of the γ subunit of *US*-$\Delta\varepsilon$*CT*-F_0F_1 relative to $\alpha_3\beta_3$ is slightly different from that of *ND*-$\Delta\varepsilon$*CT*-F_0F_1. Superimposition of the two structures with $\alpha_3\beta_3$ shows ~ 7° rotation of the γ subunit in the hydrolysis direction (Supplementary Fig. S8A). Assuming that the first ATP binds to β_{TP}, the rotation of the γ subunit driven by unisite catalysis is faint compared to the 120° rotation of the γ subunit upon binding and hydrolysis of one ATP molecule under ATP-saturated conditions (multisite conditions).

Discussion

In this study, we reveal that substoichiometric ATP is hydrolyzed at the β_{TP} of *ND*-$\Delta\varepsilon$*CT*-F_0F_1 under unisite catalysis conditions, where a single catalytic site per enzyme molecule binds ATP.

All three β subunits in *ND*-$\Delta\varepsilon$*CT*-F_0F_1 adopted an open form, implying that the first ATP can bind to any of the β subunits. Assuming that the first ATP binds to β_{TP}, the conformation change from the open to the closed form of β_{TP} occurs without the 120° rotation of γ subunit (Fig. 5A), which is consistent with previous studies suggesting unisite catalysis without rotation of γ subunit in *E. coli* F_1 (32). In the *wt*-F_0F_1 structure, ADP is bound only to β_{TP}, and both β_{DP} and β_E are in the open form without nucleotides, which suggests that β_{TP} can easily change to the closed form upon ATP binding, particularly when compared to β_{DP} and β_E. β_{TP} bound with ATP immediately changes to the closed form due to the zippering motion by the bound ATP, which likely increases the affinity of β_{TP} for ATP. This is consistent with the high affinity for ATP reported in unisite catalysis experiments (20, 22, 33). Alternatively, it is also possible that the first ATP bound to β_E and the γ subunit rotated 120° with a structural change of the ATP-bound β_E to β_{TP}, resulting in the structure of *US*-$\Delta\varepsilon$*CT*-F_0F_1. Although both catalytic pathways (Fig. 5A and B) exhibit high possibilities for unisite

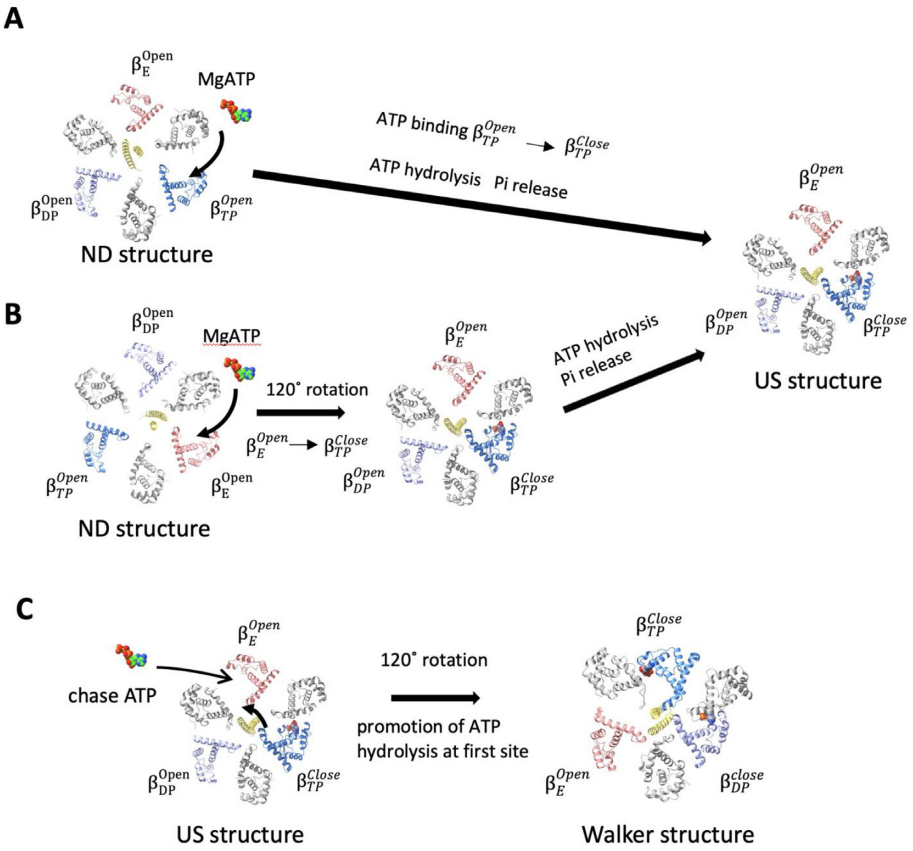

Fig. 5. Schematic representation of possible catalytic pathways for unisite catalysis at β_{TP} and promotion of ATP hydrolysis by chase ATP. Three β subunits (β_{TP}, β_{DP}, and β_E) and γ subunits are colored in blue, blue–purple, magenta and yellow, respectively. All α subunits are represented as gray. (A) First ATP binds to β_{TP} in the nucleotide-depleted (*ND*) structure where the three β subunits are open. Then, β_{TP}^{Open} changes to β_{TP}^{close} with hydrolysis of bound ATP. The conformation change of β_{TP} induces a 7° rotation of the γ subunit. The phosphate is released spontaneously, resulting in the unisite structure (*US*). (B) The first ATP binds to β_E in the *ND* structure, followed by structural changes of three β subunits with 120° rotation of the γ subunit. (C) The bound ATP on β_{TP} is slowly hydrolyzed by coordination of catalytic amino acid residues not suitable for hydrolysis of ATP. Binding of the second ATP to β_E causes 120° rotation of γ subunit and structural transition of the each of the following β subunits: β_E to β_{TP}, β_{TP} to β_{DP}, and β_{DP} to β_E. The β subunit to which the first ATP binds becomes β_{DP}, and the hydrolysis of ATP is accelerated.

catalysis, it is more likely that the first ATP binds to β_{TP} to explain the high affinity of the unisite for ATP.

Both β_{DP} and β_E retain open structures after unisite catalysis at β_{TP}; therefore, the next catalytic event is ATP binding to either β_{DP} or β_E. During ATP hydrolysis by F_0F_1, each conformational change from β_E to β_{TP}, β_{TP} to β_{DP}, and β_{DP} to β_E occurs with 120° rotation of the γ subunit. Assuming that ATP then binds to β_E and induces a conformational change of each β subunit with 120° rotation of the γ subunit, F_0F_1 adopts the following canonical Walker structure observed in most F_1 structures: "open in β_E," "closed in β_{TP} with the *second* ATP," and "closed in β_{DP} with the ADP from *first* ATP" (Fig. 5C). Several studies using various F_1-ATPases have reported that hydrolysis of ATP bound to the first catalytic site is markedly accelerated by the addition of an excess ATP (cold chase experiment) (20, 21, 35). In Walker structures, β_{TP} and β_{DP} adopt very similar closed conformations; however, their catalytic sites are not equivalent (Supplementary Fig. S10). Although these differences are relatively small, they have a marked effect on catalysis. ATP in β_{DP} is immediately hydrolyzed, whereas hydrolysis of ATP in β_{TP} proceeds slowly (14, 33). Therefore, most crystal structures of F_1 contain ATP analogs in β_{TP} and ADP in β_{DP}. Upon binding of ATP to β_E by the addition of excess ATP, the conformational change of β_{TP} to β_{DP} promoted the hydrolysis of ATP at the catalytic site (Fig. 5C).

The F_0F_1 structures exposed to 4 mM ATPγS provided direct evidence of conformational changes in the ε subunit by ATP binding in the holo-F_0F_1 complex. The retracted ε subunit in the complex contains ATP with the similar coordination as the monomeric ε subunit (Supplementary Fig. S5) (31). In another *wt*-F_0F_1 structure exposed to 4 mM ATPγS concentration, the ε-inhibited structure, which adopted "open in β_E," "closed in β_{TP}," and "open in β_{DP}," was maintained, although all nucleotide binding sites were occupied with ADP or ATPγS (Figs. 2 and 3B). This indicates that the inhibited *wt*-F_0F_1 structure by the extended ε subunit is not activated by ATP binding to β_E or β_{DP} (Fig. 2A), and that the conformational change of the ε subunit by ATP binding is crucial for the activation of *wt*-F_0F_1 for ATP hydrolysis activity (Fig. 2B).

In this study, we determined the multiple structures of F_0F_1 ATPase during catalysis by structural analysis using cryo-EM, which allows the capture of states inaccessible to crystallization. The techniques and approaches used in this study can potentially assist the elucidation of the detailed reaction and regulatory mechanisms of other enzymes.

Materials and methods

Protein purification

Wt-F_0F_1-ATP synthase from *G. stearothermophilus* was purified from *E. coli* DK 8 strain containing an expression vector (pTR19-ASDS) for F_0F_1, as described previously (24). The expression vector for $\Delta\varepsilon CT$-F_0F_1, which lacks the C-terminal of ε subunit (83 to 133 amino acids), was constructed from pTR19-ASDS. Transformed *E. coli* cells were grown in 2 × YT medium at 37°C for 16 h before harvesting by centrifugation at 5000 × *g*. The cell pellet was suspended in lysis buffer (50 mM Tris–Cl pH 8.0, 5 mM $MgCl_2$, and 10% [w/v] glycerol), and the cell membranes were collected by ultracentrifugation at 35,000 rpm for 20 min and solubilized by mixing in solubilization buffer (50 mM Tris–Cl, 5 mM $MgCl_2$, 10% [w/v] glycerol, and 2% n-dodecyl-d-maltoside [DDM]) at 4°C for 3 h. The supernatant was then applied to a Ni-NTA column. For bound nucleotide removal, the eluted fractions containing F_0F_1 were dialyzed against 200 mM sodium phosphate (pH 8.0), 10 mM EDTA, and 0.03% DDM overnight at 25°C and the dialysis buffer was changed thrice. The dialyzed F_0F_1 fractions were concentrated using ultrafiltration with an Amicon filter (100 KDa cut-off, Amicon corp.) and loaded onto a Superose 6 Increase 10/300 column (Cytiva) equilibrated with gel permeation buffer (20 mM Tris–HCl pH 8.0, 150 mM NaCl, and 0.03% DDM). The peak fractions (6 to 9 mg/mL) were used for the cryo grid preparation or ATPase assay.

Grid preparation

For cryo grid preparation, Quanfifoil R1.2/1.3 Mo grids were glow-discharged for 1 min using an Ion Bombarder (Vacuum Device). Prior to blotting, 3 μL of the samples were placed on a cryo grid and incubated for 15 min. Further, 2.6 to 3.5 μL F_0F_1 was loaded onto the grid and blotted for 3 to 10 s with a blot force of 10, drain time of 0.5 s, and 100% humidity using a FEI Vitrobot (ThermoFisher). The blotted grid was then plunged into a liquid ethane. For the unisite catalysis condition, 1 μL reaction buffer (0.2 M Tris–Cl pH 8.0, 40 μM ATP, 40 mM PEP, 1 M KCl, and 5 mg/mL pyruvate kinase) was added to 9 μL of the sample. The mixtures were incubated for 60 s at 25°C, followed by blotting and vitrification.

Cryo-EM imaging under ATPγS and *US* conditions was performed using a Titan Krios (FEI/Thermo Fisher Scientific) operating at 300 kV acceleration voltage and equipped with an electron detector K3 (Gatan) in electron counting mode (CDS). Cryo-EM imaging under *wt-ND* conditions was performed in CDS using CRYOARM 300 (JEOL) operating at 300 kV and an electron detector K3 (Gatan).

Data collection was performed using SerialEM software with a calibrated magnification of 0.88 Å pixel^{-1} for the ATPγS and $\Delta\varepsilon CT$-*US* conditions and a calibrated magnification of 1.01 Å pixel^{-1} for the *wt-ND* condition. Under *wt-ND* and ATPγS conditions, data were collected at an electron dose of 50.0 e$^-$/Å^2 for an exposure time of 5 s, and under unisite conditions, data were collected at an electron dose of 60.0 e$^-$/Å^2 for an exposure time of 6 s. The defocus range was 0.8 to 2.0 μm, and data were collected at 50 frames for the *wt-ND* condition, 55 frames for the ATPγS condition, and 59 frames for the unisite condition.

Image processing

The details of the image-processing procedure for each condition are described in Supplementary Figs. 2, 4, and 6. Image analysis was performed using RELION 4.0β (36) and cryoSPARC v3.2 (37). The file format conversion between RELION and cryoSPARC was performed using the script csparc2star.py in Pyem. The beam-induced drift was corrected using MotionCor2 (38), and the CTF was estimated using CTFFIND 4.1 (39). We analyzed 7,329 movies for the unisite condition, 9,625 movies for the *wt-ND* condition, and 17,261 movies for the ATPγS condition. Particle picking was performed using Topaz (40). Good particles were selected by 2D classification and trained using 4,000 particles. Autopicking using the trained topaz model yielded 499,788 particles for the unisite condition, 1,381,269 particles for the *wt-ND* condition, and 1,020,321 particles for the ATPγS condition. Particles picked by Topaz were subjected to 2D classification for further selection of good particles. Then heterogeneous refinements using cryoSPARC were performed to eliminate junk particles. Further, we selected 418,497 particles for unisite conditions, 622,109 particles for *wt-ND* conditions, and 912,931 particles for ATPγS conditions. Heterogeneous refinement was then used to classify F_0F_1 into multiple conformational states. These particles were re-extracted at full pixel size and subjected to repeated 3D auto-refinement, CTF refinement, and Bayesian polishing (36). The structures of the three rotational states, including their subclasses, were obtained at 3 to 4.5 Å resolution. All obtained classes of F_0F_1 were subjected to focused refinement on the F_1 part to reduce the resolution loss due to the relative motion of the F_0 part with F_1. In the analysis of the ATPγS dataset to determine a small percentage of ε-retracted structures, the class of F_0F_1 of all states were added together to increase the number of particles, and focused refinement was performed on the F_1 part. The obtained F_1 structure was subjected to focused 3D classification by masking with $\gamma\varepsilon$-β_{DP} to detect structural changes between the ε and β subunits. The resolution was estimated using the gold standard Fourier shell correlation (FSC) = 0.143 criterion.

Model building and refinement

We used Phenix real-space refinement (41), ISOLDE (42), and COOT (41) for the atomic model building. The epsilon-extended F_1 model was built using PDB 6N2Y as the initial model, and the epsilon-retracted subunit was built using PDB 2E5Y. The initial model, which was a rigid body fitted to the density map by UCSF ChimeraX (43), was first refined by Phenix real-space refinement. Residues that did not fit correctly into the map were manually placed using the COOT and ISOLDE. Refinement and manual modification were repeated until the model parameters were improved. Lastly, the refinement model was evaluated using MolProbity (44) and EMRinger (45).

Acknowledgments

We are grateful to all the members of the Yokoyama Lab for their continuous support and technical assistance. We also thank Prof. Allison for his enthusiastic discussion on unisite catalysis long time ago.

Supplementary materials

Supplementary materials are available at *PNAS Nexus* online.

Funding

Our research was supported by Grant-in-Aid for Scientific Research (JSPS KAKENHI) Grant Number 20H03231 to K.Y., 20K06514 to J.K., and Grant-in-Aid for JSPS Fellows Grant Number 20J00162 to A.N., and Takeda Science foundation to K.Y. Our research was

also supported by Platform Project for Supporting Drug Discovery and Life Science Research (Basis for Supporting Innovative Drug Discovery and Life Science Research [BINDS]) from AMED under Grant Number JP17am0101001 (support number 1312), Grants-in-Aid from "Nanotechnology Platform" of the Ministry of Education, Culture, Sports, Science and Technology (MEXT) to K.M. (Project Number. 12024046), and the Research Program for Next Generation Young Scientists of "Five-star Alliance" in "NJRC Mater. & Dev." under Grant Number 20215008 to A.N..

Authors' contributions

K.Y., J.K., A. Nakanishi, and A. Nakano designed, performed, and analyzed the experiments; A. Nakano analyzed the data and contributed to the preparation of the samples; J.K. and K.M. provided technical support and conceptual advice; and K.Y. designed and supervised the experiments and wrote the manuscript. All authors discussed the results and commented on the manuscript.

Data availability

Data is available in the manuscript and supplementary materials. Cryo-EM density maps (.mrc files) and atomic models (.pdb files) obtained in this study were deposited to EMDB and PDB. The accession codes (PDBID and EMDBID) 7XKH, 7XKQ, 7XKR, 7XKO, 7XKP, 33,251, 33,252, 33,253, 33,264, 33,265, 33,266, 33,267, 33,268, 33,277, 33,258, 33,278, 33,259, 33,279, 33,260, 33,280, 33,261, 33,281, 33,269, 33,282, 33,262, 33,283, and 33,263 are summarized in Supplementary Tables S2–S5. The data that support the findings of this study are available from PDB and EMDB.

References

1. Kühlbrandt W. 2019. Structure and mechanisms of F-type ATP synthases. Annu Rev Biochem 88:515–549.
2. Boyer PD. 1997. The ATP synthase—a splendid molecular machine. Annu Rev Biochem 66:717–749.
3. Yoshida M, Muneyuki E, Hisabori T. 2001. ATP synthase—a marvellous rotary engine of the cell. Nat Rev Mol Cell Biol 2:669–677.
4. Noji H, Yasuda R, Yoshida M, Kinosita K, Jr. 1997. Direct observation of the rotation of F_1-ATPase. Nature 386:299–302.
5. Yasuda R, Noji H, Yoshida M, Kinosita K, Jr., Itoh H. 2001. Resolution of distinct rotational substeps by submillisecond kinetic analysis of F_1-ATPase. Nature 410:898–904.
6. Imamura H, *et al.* 2003. Evidence for rotation of V1-ATPase. Proc Natl Acad Sci U S A 100:2312–2315.
7. Yanagisawa S, Frasch WD. 2021. pH-dependent 11°F_1F_0 ATP synthase sub-steps reveal insight into the F_0 torque generating mechanism. eLife 10:e70016.
8. Spetzler D, *et al.* 2006. Microsecond time scale rotation measurements of single F_1-ATPase molecules. Biochemistry 45:3117–3124.
9. Adachi K, *et al.* 2007. Coupling of rotation and catalysis in F(1)-ATPase revealed by single-molecule imaging and manipulation. Cell 130:309–321.
10. Adachi K, Oiwa K, Yoshida M, Nishizaka T, Kinosita K, Jr. 2012. Controlled rotation of the F_1-ATPase reveals differential and continuous binding changes for ATP synthesis. Nat Commun 3:1022.
11. Diez M, *et al.* 2004. Proton-powered subunit rotation in single membrane-bound F_0F_1-ATP synthase. Nat Struct Mol Biol 11:135–141.
12. Guo H, Suzuki T, Rubinstein JL. 2019. Structure of a bacterial ATP synthase. eLife 8:e43128.
13. Abrahams JP, Leslie AG, Lutter R, Walker JE. 1994. Structure at 2.8-A resolution of F_1-ATPase from bovine heart mitochondria. Nature 370:621–628.
14. Menz RI, Leslie AG, Walker JE. 2001. Structure of bovine mitochondrial F(1)-ATPase with nucleotide bound to all three catalytic sites: implications for the mechanism of rotary catalysis. Cell 106(3):331–341.
15. Suzuki K, *et al.* 2016. Crystal structures of the ATP-binding and ADP-release dwells of the V(1) rotary motor. Nat Commun 7:13235.
16. Arai S, *et al.* 2013. Rotation mechanism of *Enterococcus hirae* V1-ATPase based on asymmetric crystal structures. Nature 493:703–707.
17. Nakanishi A, Kishikawa JI, Tamakoshi M, Mitsuoka K, Yokoyama K. 2018. Cryo EM structure of intact rotary H(+)-ATPase/synthase from *Thermus thermophilus*. Nat Commun 9:89.
18. Jault JM, Allison WS. 1994. Hysteretic inhibition of the bovine heart mitochondrial F_1-ATPase is due to saturation of noncatalytic sites with ADP which blocks activation of the enzyme by ATP. J Biol Chem 269:319–325.
19. Sakaki N, *et al.* 2005. One rotary mechanism for F_1-ATPase over ATP concentrations from millimolar down to nanomolar. Biophys J 88:2047–2056.
20. Grubmeyer C, Cross RL, Penefsky HS. 1982. Mechanism of ATP hydrolysis by beef heart mitochondrial ATPase. Rate constants for elementary steps in catalysis at a single site. J Biol Chem 257:12092–12100.
21. Yokoyama K, Hisabori T, Yoshida M. 1989. The reconstituted $\alpha_3\beta_3\delta$ complex of the thermostable F_1-ATPase. J Biol Chem 264:21837–21841.
22. Konishi J, Yohda M, Hashimoto T, Yoshida M. 1987. Single site catalysis of the F_1-ATPase from *Saccharomyces cerevisiae* and the effect of inorganic phosphate on it. J Biochem 102: 273–279.
23. Hisabori T, *et al.* 1992. Single site hydrolysis of 2′,3′-O-(2,4,6-trinitrophenyl)-ATP by the F_1-ATPase from thermophilic bacterium PS_3 is accelerated by the chase-addition of excess ATP. J Biol Chem 267:4551–4556.
24. Suzuki T, Ueno H, Mitome N, Suzuki J, Yoshida M. 2002. F(0) of ATP synthase is a rotary proton channel. Obligatory coupling of proton translocation with rotation of c-subunit ring. J Biol Chem 277:13281–13285.
25. Kato S, Yoshida M, Kato-Yamada Y. 2007. Role of the epsilon subunit of thermophilic F_1-ATPase as a sensor for ATP. J Biol Chem 282:37618–37623.
26. Shirakihara Y, *et al.* 2015. Structure of a thermophilic F_1-ATPase inhibited by an ε-subunit: deeper insight into the ε-inhibition mechanism. FEBS J 282:2895–2913.
27. Suzuki T, *et al.* 2003. F_0F_1-ATPase/synthase is geared to the synthesis mode by conformational rearrangement of epsilon subunit in response to proton motive force and ADP/ATP balance. J Biol Chem 278:46840–46846.
28. Tsunoda SP, *et al.* 2001. Large conformational changes of the epsilon subunit in the bacterial F_1F_0-ATP synthase provide a ratchet action to regulate this rotary motor enzyme. Proc Natl Acad Sci U S A 98:6560–6564.
29. Imamura H, *et al.* 2009. Visualization of ATP levels inside single living cells with fluorescence resonance energy transfer-based genetically encoded indicators. Proc Natl Acad Sci U S A 106:15651–15656.
30. Imamura H, *et al.* 2005. Rotation scheme of V_1-motor is different from that of F_1-motor. Proc Natl Acad Sci U S A 102: 17929–17933.

31. Yagi H, *et al.* 2007. Structures of the thermophilic F_1-ATPase epsilon subunit suggesting ATP-regulated arm motion of its C-terminal domain in F_1. Proc Natl Acad Sci U S A 104:11233–11238.
32. García JJ, Capaldi RA. 1998. Unisite catalysis without rotation of the γ-ε domain in *Escherichia coli* F_1-ATPase. J Biol Chem 273:15940–15945.
33. Al-Shawi MK, Senior AE. 1988. Complete kinetic and thermodynamic characterization of the unisite catalytic pathway of *Escherichia coli* F_1-ATPase. Comparison with mitochondrial F_1-ATPase and application to the study of mutant enzymes. J Biol Chem 263:19640–19648.
34. Senior AE. 1992. Catalytic sites of *Escherichia coli* F_1-ATPase. J Bioenerg Biomembr 24:479–484.
35. Amano T, Tozawa K, Yoshida M, Murakami H. 1994. Spatial precision of a catalytic carboxylate of F_1-ATPase beta subunit probed by introducing different carboxylate-containing side chains. FEBS Lett 348:93–98.
36. Scheres SH. 2012. RELION: implementation of a Bayesian approach to cryo-EM structure determination. J Struct Biol 180:519–530.
37. Punjani A, Rubinstein JL, Fleet DJ, Brubaker MA. 2017. cryoSPARC: algorithms for rapid unsupervised cryo-EM structure determination. Nat Methods 14:290–296.
38. Zheng SQ, *et al.* 2017. MotionCor2: anisotropic correction of beam-induced motion for improved cryo-electron microscopy. Nat Methods 14:331–332.
39. Rohou A, Grigorieff N. 2015. CTFFIND4: fast and accurate defocus estimation from electron micrographs. J Struct Biol 192:216–221.
40. Bepler T, *et al.* 2019. Positive-unlabeled convolutional neural networks for particle picking in cryo-electron micrographs. Nat Methods 16:1153–1160.
41. Liebschner D, *et al.* 2019. Macromolecular structure determination using X-rays, neutrons and electrons: recent developments in Phenix. Acta Crystallogr D Struct Biol 75:861–877.
42. Croll TI. 2018. Isolde: a physically realistic environment for model building into low-resolution electron-density maps. Acta Crystallogr D Struct Biol 74:519–530.
43. Pettersen EF, *et al.* 2021. UCSF ChimeraX: Structure visualization for researchers, educators, and developers. Protein Sci 30:70–82.
44. Barad BA, *et al.* 2015. EMRinger: side chain-directed model and map validation for 3D cryo-electron microscopy. Nat Methods 12:943–946.
45. Chen VB, *et al.* 2010. MolProbity: all-atom structure validation for macromolecular crystallography. Acta Crystallogr D Biol Crystallogr 66:12–21.